

A Flexible, 2.4-GHz Wireless Ion Sensor System Using Printed Organic Amplifiers with 3-V Single Supply

Rei Shiwaku,* Hiroyuki Matsui,* Yuki Hommura, Yasunori Takeda, Kuniaki Nagamine, and Shizuo Tokito*

Integration of organic thin-film transistor (OTFT) devices with a wireless data transmission system such as 2.4-GHz Bluetooth low energy (BLE) is a significant requirement for activating the Internet of Thing (IoT) ecosystem based on a vast number of sensors, while conventional OTFT circuits have problems with their high output impedance and the need for multiple power supplies. Here, a wireless, real-time, and flexible sodium ion sensing system composed of a printed Na⁺ sensor, printed OTFT-based amplifiers, inorganic passive elements, a BLE module, and a 3-V sheet-type battery is demonstrated. The printed organic amplifier circuits based on dual threshold technology and dual-gate structure are combinable with a BLE module because of their low output impedance of 50 k Ω and operate with 3-V single supply as well as improving operational stability under illumination. The sensitivity to Na⁺ concentration is improved from 53.7 to 242.5 mV dec⁻¹ (4.5 times higher) by the OTFT-based amplifier, and the data is transmitted in real-time to a tablet via the BLE wireless communication.

OTFTs can exhibit extreme mechanical flexibility^[2] and all their layers such as gate, source, and drain (SD) electrodes, gate dielectrics, insulating layers, and organic semiconductor (OSC) layers can be fabricated by using printing methods at maximum process temperatures below 150°C.^[3,4] Taking advantage of the characteristics of OTFTs, there has been considerable work on their applications to amplifiers for physical sensors (e.g., electromyogram,^[5] electrocardiogram,^[6,7] pulse,^[8] and temperature^[9]) and for bio-chemical sensors (e.g., metabolites,^[10] electrolytes,^[11] proteins,^[12] and ribonucleic acids^[13]) toward real-time and continuous acquiring of vital and physiological information in the field of healthcare, sports and medicals.

Organic amplifier circuits are often composed of depletion-load p-type

metal-oxide-semiconductor (PMOS) inverter circuits on the basis of the dual threshold technology,^[14,15] which requires two types of TFTs, e.g., normally-off TFTs whose threshold voltage (V_{TH}) is low ($V_{TH} < 0$ V) and normally-on TFTs ($V_{TH} > 0$ V).^[16] The advantage of the dual threshold technology utilizing control of V_{TH} is to enable optimization of the noise margin, amplification gain, and operation speed of the circuits, with high degree of freedom of the circuit design, compared to single threshold design without control of V_{TH} .^[15,17] To maximize circuit performances and obtain dual V_{TH} , several promising methods for controlling V_{TH} based on material engineering (e.g., gate electrodes,^[14,15] gate dielectrics,^[17] binder for organic semiconductor inks^[18]), interface engineering (e.g., SD electrodes/OSC,^[19] dielectric/OSC,^[20] gate/dielectric^[21]), and geometry engineering (e.g., channel pattern,^[22] dual-gate structure,^[23] tri-gate structure^[24]) have been previously reported; however, these methods required the specific materials/process technology, which potentially limits a choice of methods for controlling V_{TH} or complicates the whole device process, although the process should be simple and applicable for various printing methods.

Integration of organic amplifiers with a wireless data transmission system is an essential requirement for activating the IoT ecosystem. A few studies on OTFT-based wireless devices with 13.56-MHz band have been reported.^[25,26] On the other hand, there is no report on integrating organic amplifiers and wireless transmission assemblies such as Bluetooth Low Energy (BLE)

1. Introduction

Printed electronics, which enable vacuum-free, large-area, highly customizable, and eco-friendly manufacturing of electronic devices, have been the promising technology for laying the foundations of the Internet of Things (IoT) ecosystem society based on a vast number of sensors connected with wired or wireless communication networks.^[1] One of the fundamental active electronic elements in printed electronics is organic thin-film transistors (OTFTs) that are essential for signal processing.

R. Shiwaku

Functional Polymers Research Laboratory

Tosoh Corporation

1-8 Kasumi, Yokkaichi, Mie 510-8540, Japan

E-mail: rei-shiwaku-tj@tosoh.co.jp

H. Matsui, Y. Hommura, Y. Takeda, K. Nagamine, S. Tokito

Research Center for Organic Electronics (ROEL)

Yamagata University

4-3-16 Jonan, Yonezawa, Yamagata 992-8510, Japan

E-mail: h-matsui@yz.yamagata-u.ac.jp; tokito@yz.yamagata-u.ac.jp

 The ORCID identification number(s) for the author(s) of this article can be found under <https://doi.org/10.1002/aelm.202300396>

© 2023 The Authors. Advanced Electronic Materials published by Wiley-VCH GmbH. This is an open access article under the terms of the Creative Commons Attribution License, which permits use, distribution and reproduction in any medium, provided the original work is properly cited.

DOI: 10.1002/aelm.202300396

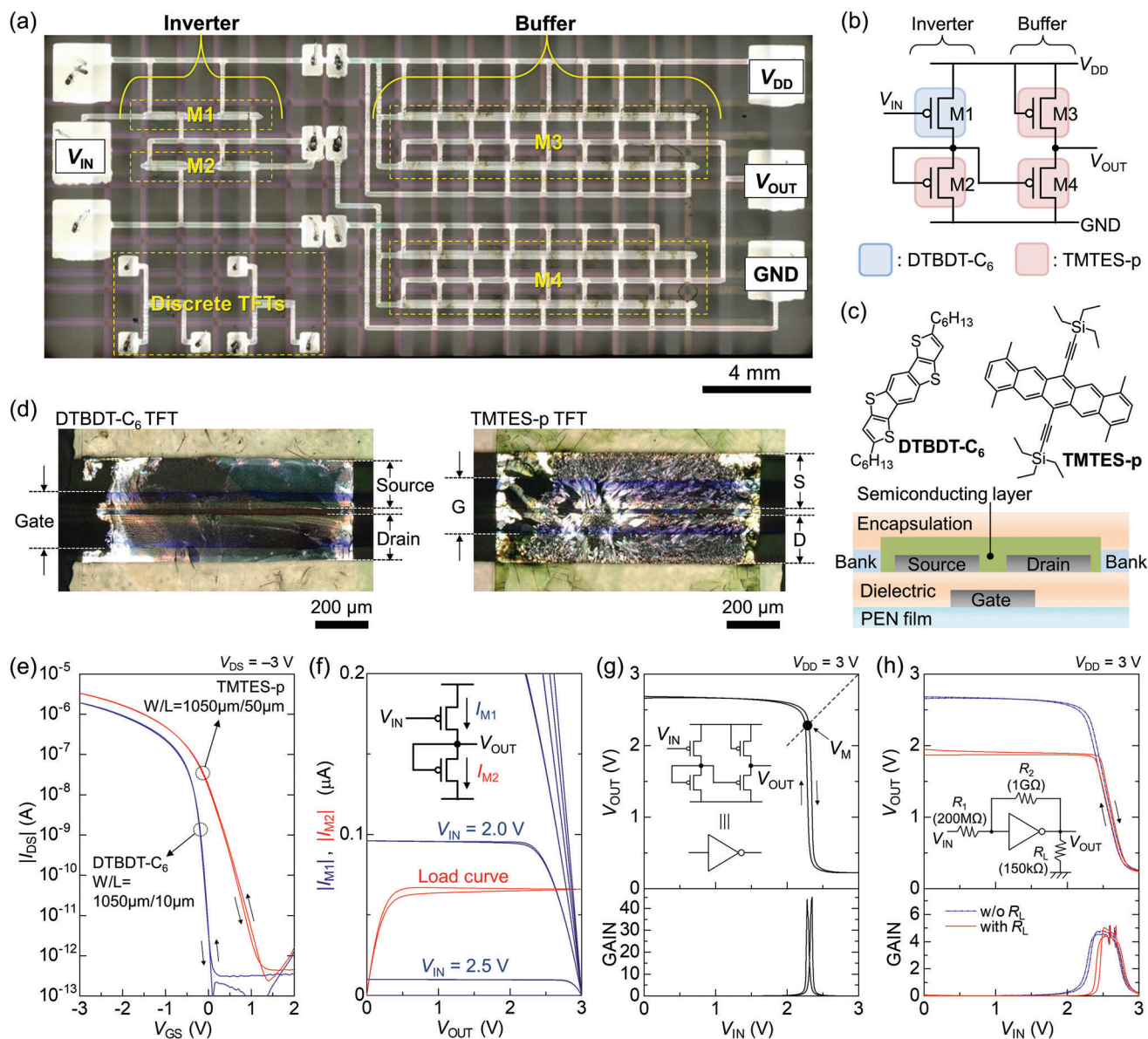


Figure 1. Design, structure, and electrical characteristics of the printed OTFT devices. a) Optical microscope image of the OTFT device. b) Circuit diagram of the amplifier. c) Schematics of the OTFT structure. d) Cross-polarized microscope images of the OTFT channel region. e) Transfer, f) output characteristics of the OTFTs. Output curves of the drive OTFT (I_{M1} , blue lines) and the characteristics of the load OTFT (I_{M2} , red line) as functions of V_{OUT} . V_{DS} in the drive OTFT converted by $V_{OUT} = V_{DD} + V_{DS}$. Static input-output characteristics of the amplifier g) without and h) with a negative-feedback as well as a load resistance. The dashed black line represents the line $V_{IN} = V_{OUT}$.

modules for real-time data monitoring, because of high output impedance of organic amplifiers. Output impedance of an organic amplifier ($Z_{OUT(AMP)}$) should be sufficiently lower than input impedance of a BLE module ($Z_{IN(BLE)}$, typically $\approx 150 \text{ k}\Omega$) to minimize attenuation in voltage transmitted from a BLE module (V_{BLE}), considering that V_{BLE} is given by (for details, see Figure S4, Supporting Information):

$$V_{BLE} = \frac{Z_{IN(BLE)}}{Z_{OUT(AMP)} + Z_{IN(BLE)}} V_{OUT(AMP)} \quad (1)$$

where $V_{OUT(AMP)}$ is output voltage of the organic amplifier. One typical output impedance in organic amplifiers is $\approx 5 \text{ M}\Omega$,^[15] which leads to attenuation in V_{BLE} by a factor of ≈ 100 , according to Equation (1). Additionally, taking account of the background in which charge carrier mobilities in OTFTs are one or two orders of magnitude lower than those of silicon-based TFTs,^[27,28] reduction of $Z_{OUT(AMP)}$ below $150 \text{ k}\Omega$ is, therefore, a significant issue.

In this work, we demonstrate the operation of the flexible integrated potentiometric sensor (FIPS) device composed of a printed sodium ion (Na^+) sensor, printed organic amplifiers, a BLE module, and a 3-V sheet-type battery. As the dual threshold

technology suitable for printed electronics, we employed two organic semiconductor materials, 2,7-dihexyl-dithieno[2,3-d;2',3'-d']benzo[1,2-b;4,5-b']dithiophene (DTBDT-C₆) for the normally-off TFT channels and 1,4,8,11-tetramethyl-6,13-bis(triethylsilylethynyl)pentacene (TMTES-p) for the normally-on TFT channels. These semiconductor materials were printed on flexible film substrates to fabricate the depletion-load inverter (INV) circuits. Taking full advantage of the normally on characteristics of the TMTES-p TFTs, a common-drain voltage buffer (BF) circuit was also fabricated and integrated with the INV circuit to reduce $Z_{OUT(AMP)}$. The organic amplifier based on the INV and BF circuits were combinable with a BLE module because of their low output impedance of 50 k Ω and were operable with 3-V single supply. Additionally, to improve electrical performances of the organic amplifiers, dual-gate (DG) structure was applied to the OTFT devices and we obtained improved INV gain as well as operational stability of the OTFT device under illumination. Wireless, real-time potentiometric sensing was successfully demonstrated with the developed FIPS device; the sensitivity of the potentiometric Na⁺ sensor was improved from 53.7 to 242.5 mV dec⁻¹ (4.5 times higher) by the organic amplifier and the data was transmitted to a tablet without significant signal attenuation.

2. Results and Discussion

2.1. Printed Organic Amplifier Circuits with Dual Threshold Technology

The schematic illustration of the fabricated OTFT devices is displayed in Figure 1c. All layers except for the gate dielectric and the encapsulation layer were formed by printing processes at process temperatures below 120 °C on a 100- μ m-thick polyethylene naphthalate (PEN) film substrate (The process flow is shown in Figure S1, Supporting Information). The electrodes were fabricated by inkjet printing of silver nanoparticle ink. A fluoropolymer bank layer and the semiconductor layer were printed by a dispenser equipment. The bank layer was used to define the channel width precisely and also to control the crystal growth of the organic semiconductor, which leads to the uniform morphology (Figure 1d).^[12] Blend solutions of the organic semiconductor (DTBDT-C₆^[29] and TMTES-p^[30]) and polystyrene were used as the active layer to obtain uniform electrical performances.^[16] A parylene gate dielectric (100 nm thick) and encapsulation layer (1 μ m thick) were formed by chemical vapor deposition.

The transfer characteristics of the OTFTs in a saturation regime are shown in Figure 1e, indicating dual threshold voltages were successfully prepared. For the DTBDT-C₆ OTFTs, the mobility of 0.5 (\pm 0.1) cm² V⁻¹ s⁻¹, threshold voltage of -0.17 (\pm 0.04) V, and subthreshold slope of 79 (\pm 9) mV dec⁻¹ were obtained at supply voltage of -3 V and dielectric capacitance per unit area of 36.5 nF cm⁻². For the TMTES-p OTFTs, the mobility of 1.7 (\pm 0.6) cm² V⁻¹ s⁻¹, threshold voltage of 0.28 (\pm 0.14) V, and subthreshold slope of 260 (\pm 7) mV dec⁻¹ were obtained. The semiconductor/electrode contact was Ohmic rather than Schottky, according to the output curve in the linear regime shown in Figure 1f.

The circuit diagram of the fabricated amplifier is displayed in Figure 1b. The first and second stages are a depletion-load in-

verter (INV) for getting high gain and a common-drain voltage buffer (BF) circuit for obtaining low output impedance, respectively. An organic semiconductor DTBDT-C₆ was used for the channel material of the drive TFT (M1) whose electrical characteristic should be normally off ($V_{TH} < 0$ V), and TMTES-p was used for the channel material of the TFTs whose electrical characteristics should be normally-on ($V_{TH} > 0$ V), such as the load TFT (M2) and TFTs that compose the BF circuit (M3, M4). The circuits in this work could be driven by single power supply, while pseudo-CMOS^[31] that was previously designed for reducing output impedance requires dual power supplies. Figure 1a displays the optical microscope image of the amplifier circuit. The channel width/length of M1, M2, M3 and M4 was 2 000 μ m/30 μ m, 2 000 μ m/50 μ m, 16 000 μ m/10 μ m and 16 000 μ m/10 μ m, respectively.

The representative static input-output characteristic of the amplifier based on the INV and BF circuits at supply voltage of $V_{DD} = 3$ V is displayed in Figure 1g, showing open-loop gain of ≈ 45 . Switching voltage (V_M) defined as the crossing point of the static input-output characteristics of the amplifier and the line $V_{IN} = V_{OUT}$ was 2.3 V, which is consistent with a value estimated from the output curves of the M1 and M2 as functions of V_{OUT} in Figure 1f.^[16] Here the V_{DS} of the M1 corresponds to $V_{OUT} - V_{DD}$ of the INV, that is, $V_{OUT} = V_{DS} + V_{DD}$. Since the currents in M1 and M2 should be equal to each other, the crossing point of the two curves at bottom axis gives V_{OUT} of the INV. Figure 1f indicates that the crossing point switches quickly when the input voltage is changed from 2.0 to 2.5 V, which results in a high INV gain. The closed-loop gain of the amplifier was controlled to ≈ 4.3 by a negative-feedback using two resistors ($R_1 = 200$ M Ω , $R_2 = 1$ G Ω), as shown in Figure 1h. The closed-loop gain of the amplifier with the negative feedback is expressed as follows:^[11]

$$\text{Gain} = \frac{R_2}{R_1 + \frac{R_1 + R_2}{A_{\text{open}}}} \quad (2)$$

where A_{open} is the open-loop gain of the INV. The formula indicates that the closed-loop gain can be controlled by the two resistors.

BF circuits play a crucial role in integration of OTFT-based circuits and a BLE module. If the BF circuit is not integrated with the INV circuit, V_{OUT} of the INV circuit drops considerably when the INV is connected with a BLE module; consequently, signals cannot be transmitted to an external device via BLE communication (see Figure S4, Supporting Information). Output impedance of the OTFT-based circuits should be reduced for minimizing a drop in V_{OUT} , according to Equation (1). Figure S5 (Supporting Information) shows static input-output characteristics of the INV circuit with and without the BF circuit. Output impedance of the circuit was reduced from 12.5 M Ω to 20.6 k Ω (three orders of magnitude lower) by the BF circuit. A drop in V_{OUT} of the INV circuit was 83% when a 150-k Ω load resistance (a typical value of input impedance of BLE modules) was connected with the output terminal, while a drop in V_{OUT} of the INV with the BF was 17%, obviously indicating the BF is an essential circuit toward connecting OTFT-based circuits with a BLE module.

To estimate output impedance of the amplifier, a 150-k Ω load resistance was connected with the output terminal of the ampli-

Table 1. Comparison of output impedance and supply voltage in organic amplifiers.

Ref.	Circuit Design	Fabrication Method	Semiconductor Materials	Output Impedance	Supply Voltage
This work	PMOS depletion-load inverter & common-drain buffer	Digital printing	DTBDT-C ₆ , TMTES-pentacene	50 kΩ	3 V (single)
[10]	Pseudo-CMOS depletion-load	Digital printing	DTBDT-C ₆	100–300 kΩ	3, 4 V (dual)
[15]	PMOS depletion-load inverter & common-drain buffer	Photolithography	Pentacene	5 MΩ	5 V (single)

fier (Inset in Figure 1h). V_{OUT} dropped by 0.7 V as shown in Figure 1h, which is in approximate agreement with a value estimated using LT-spice simulation (Figure S6, Supporting Information). Output impedance of the organic amplifier circuits is given by: $Z_{OUT(AMP)} = \frac{R_L}{V_L} (V - V_L)$, where R_L is load-resistance, V is output voltage without R_L , and V_L is output voltage with R_L . $Z_{OUT(AMP)}$ was estimated to be ≈ 50 kΩ, which is comparable with a value from LT-spice simulation (Figure S6, Supporting Information) and is 33% value of input impedance of a BLE module, indicating that the organic amplifier was connectable with a BLE module without a considerable drop in V_{OUT} of the organic amplifier. **Table 1** compares the output impedance of the organic amplifiers and power supply with the others in the literature, suggesting that the output impedance low enough to connect to a BLE module was achieved for the first time at practical 3-V single supply in organic amplifiers.

2.2. Improvement of Amplifier Gain and Light-Shielding with Dual-Gate Structure

To improve electrical performances of the organic amplifiers, dual-gate (DG) structure was applied to the OTFT devices. Higher amplifier gain are expected by using DG structure than single-gate (SG), because applying a second voltage bias improves controllability of charge carrier density in organic semiconductor layers,^[32] which enables improved transconductance^[33] and drain current more saturated,^[34] finally contributing to increase in gain of amplifiers.^[34,35] On the other hand, we also expected improvement of operational stability under illumination because its two electrodes (bottom- and top-gate electrodes) act as light-shielding layers. The OTFT devices with SG structure (**Figure 2b**) and DG structure (**Figure 2c**) were fabricated on the same substrate and electrical measurement under illumination was performed as a facile test of light-shielding whose scheme is as follows: first was measured in dark, and second was measured under white LED light exposure (exposure time: 90 s), then the final measurement in dark again was started within 10 s after the previous measurement (**Figure 2a**).

The static input-output characteristics of the amplifier circuits with SG and DG structures are shown in **Figure 2d,f**, respectively. Gain of the DG devices (≈ 30) was higher than that of the SG device (≈ 10) before the LED light exposure due to the second voltage bias.^[32–35] Under the LED light, the gain decreased to 40% of the initial value for the SG devices, while 67% of the initial value for the DG devices was observed. Then, carrying out electrical measurements in dark again, the gain recovered up to 50%

of the initial value for the SG devices, whereas 80% of the initial value for the DG devices was observed. The results indicate that photo-induced degradation of the OTFT devices was suppressed by light-shielding with DG structure. Nevertheless, small change in the characteristics of the DG devices were still observed. Possible reason for this small change is that the top-gate electrodes slightly transmitted the LED light and the light reached the semiconductor layer through the top-gate electrode. Further improvement of the stability under illumination may be required in the future, e.g., increasing thickness of the top-gate electrodes or fabricating the top-gate electrode based on a low transmittance material such as carbon black.

Transfer characteristics of the OTFTs with SG and DG structure are shown in **Figure 2e,g**. Measuring in dark after the light exposure, a decrease in on current (I_{ON}) was 7% from the initial value for the SG DTBDT-C₆ TFTs (top of **Figure 2e**), while a decrease in I_{ON} was <2.5% for the DG DTBDT-C₆ TFTs (top of **Figure 2g**). On the other hand, an increase in I_{ON} was 32% from the initial value for the TMTES-p SG-TFTs (bottom of **Figure 2e**), while an increase in I_{ON} was 18% from the initial value for the TMTES-p DG-TFTs (bottom of **Figure 2g**). The stability in I_{ON} under illumination was improved for the TMTES-p TFTs rather than for the DTBDT-C₆ TFTs. We consider that the difference in this kind of improvement between DTBDT-C₆ and TMTES-p TFTs was attributed to difference in their band gaps (BGs) and the highest occupied molecule orbitals (HOMOs) between DTBDT-C₆ (BG: 3.92 eV, HOMO: 5.42 eV)^[29] and TMTES-p (BG: 1.87 eV, HOMO: 5.19–5.39 eV).^[30] Assuming that narrower BGs and shallower HOMOs (a feature of organic semiconductor materials desirable for getting normally-on OTFTs) contributes to generation of photo-carriers,^[36] TMTES-p was more sensitive to illumination than DTBDT-C₆; therefore, the improvement figured more prominently for the TMTES-p TFTs rather than for the DTBDT-C₆ TFTs.

2.3. Demonstration of Wireless Na⁺ Sensing Using Organic Amplifiers

To demonstrate the operation of the wireless sensor device including the organic amplifiers, the FIPS device was fabricated based on a printed sodium ion (Na⁺) sensor, the printed organic amplifiers, a BLE module, passive elements, and a 3-V sheet-type lithium-ion battery, as shown in **Figure 3b**. The Na⁺ sensor was composed of two electrodes: an ion-selective electrode (ISE) with ionophores and a reference electrode (RE). The Na⁺ sensor was fabricated by a printing method (The process flow

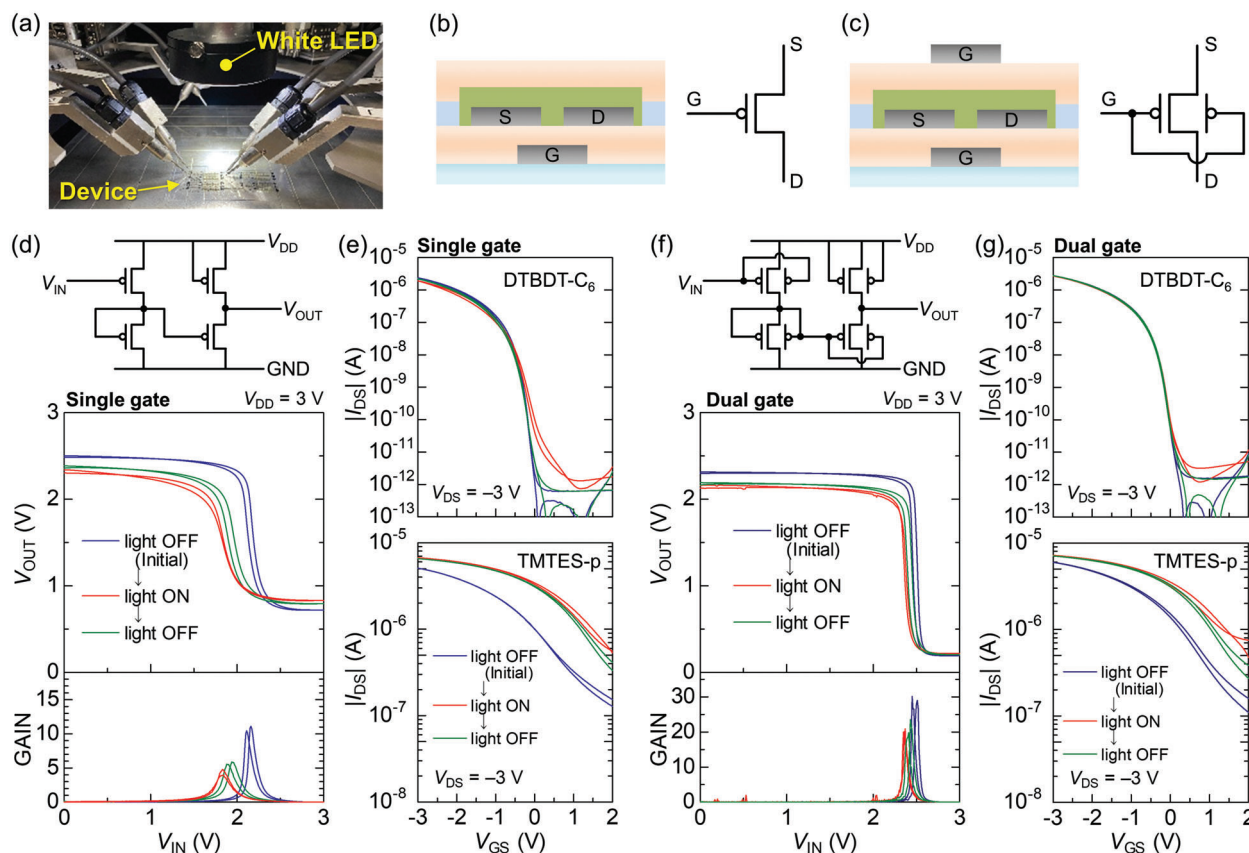


Figure 2. Suppression of the OTFT device photo-sensitivity by light-shielding with dual-gate architecture. a) Photograph of the electrical measurement under illumination. Schematics (right) and circuit diagrams (left) of the OTFT with b) single-gate (SG) and c) dual-gate (DG) structure. The bottom- and top-gate electrodes of the DG devices were connected to each other. Circuit diagrams (top) and static input-output transfer characteristics (bottom) of the amplifier circuit with d) SG and f) DG structure. Transfer characteristics of the DTBBDT-C₆ (top) and TMTES-p (bottom) OTFTs with e) SG and g) DG structure.

is shown in Figure S2, Supporting Information) and used as an electrochemical potentiometric sensor. The voltage between the ISE and RE, E , varies with the activity (or concentration for a dilute solution) of Na⁺, a_{Na^+} (or [Na⁺]), according to the Nernst equation: $E = E^0 + \frac{RT}{F} \ln a_{\text{Na}^+}$, where E^0 is the standard potential, R is the ideal gas constant, T is the temperature, and F is the Faraday constant. Hence, the sensitivity is usually evaluated by $\frac{dE}{d(\log[\text{Na}^+])}$ in units of V dec⁻¹. The amplification system that was previously developed for potentiometry^[11] was used as shown in Figure 3b. The system includes an amplification unit (AMP) and a reference unit (REF), which requires the two organic amplifiers. An optimum pair of the organic amplifier was chosen and used for the system. Passive elements (resistors and capacitors) and a BLE module were mounted on another polyimide film substrate. The photograph of the entire experiment system is shown in Figure 3a. The Na⁺ sensor was dipped in NaCl aqueous solution in a beaker, and the signal was transmitted from the FIPS device to a tablet via BLE wireless communication. We note that the small changes in characteristics of the OTFT devices were observed despite using DG structure as shown in Figure 2f; thus, the organic amplifiers were covered with aluminum foil as additional light-shielding.

The response of the Na⁺ sensor in potentiometric measurements was first tested using a commercial potentiostat. When concentrated NaCl aqueous solution was added, the potential of the Na⁺ sensor (V_{Pot}) changed stepwise over several seconds as shown in Figure 3c. The calibration (Inset in Figure 3c) indicated the sensitivity was 53.7 mV dec⁻¹, which is nearly consistent with the theoretical value of 59 mV dec⁻¹. Figure 3d shows the voltage data transmitted from the FIPS device (V_{FIPS}) to a tablet. The calibration (Inset in Figure 3d) indicated the sensitivity was -242.5 mV dec⁻¹. Figure 3e shows the change in V_{FIPS} as a function of the change in V_{Pot} . The slope of the line was estimated to be 4.5, in excellent agreement with the predefined amplification factor in Figure 1h. Thus, the wireless potentiometric sensing was successfully demonstrated with the FIPS devices.

3. Conclusion

We successfully demonstrated wireless, real-time Na⁺ sensing with the flexible integrated potentiometric sensor (FIPS) device comprised of a printed Na⁺ sensor, the organic amplifier circuits, inorganic passive elements, a BLE module, and a 3-V sheet-type lithium-ion battery. The printed organic amplifier circuits

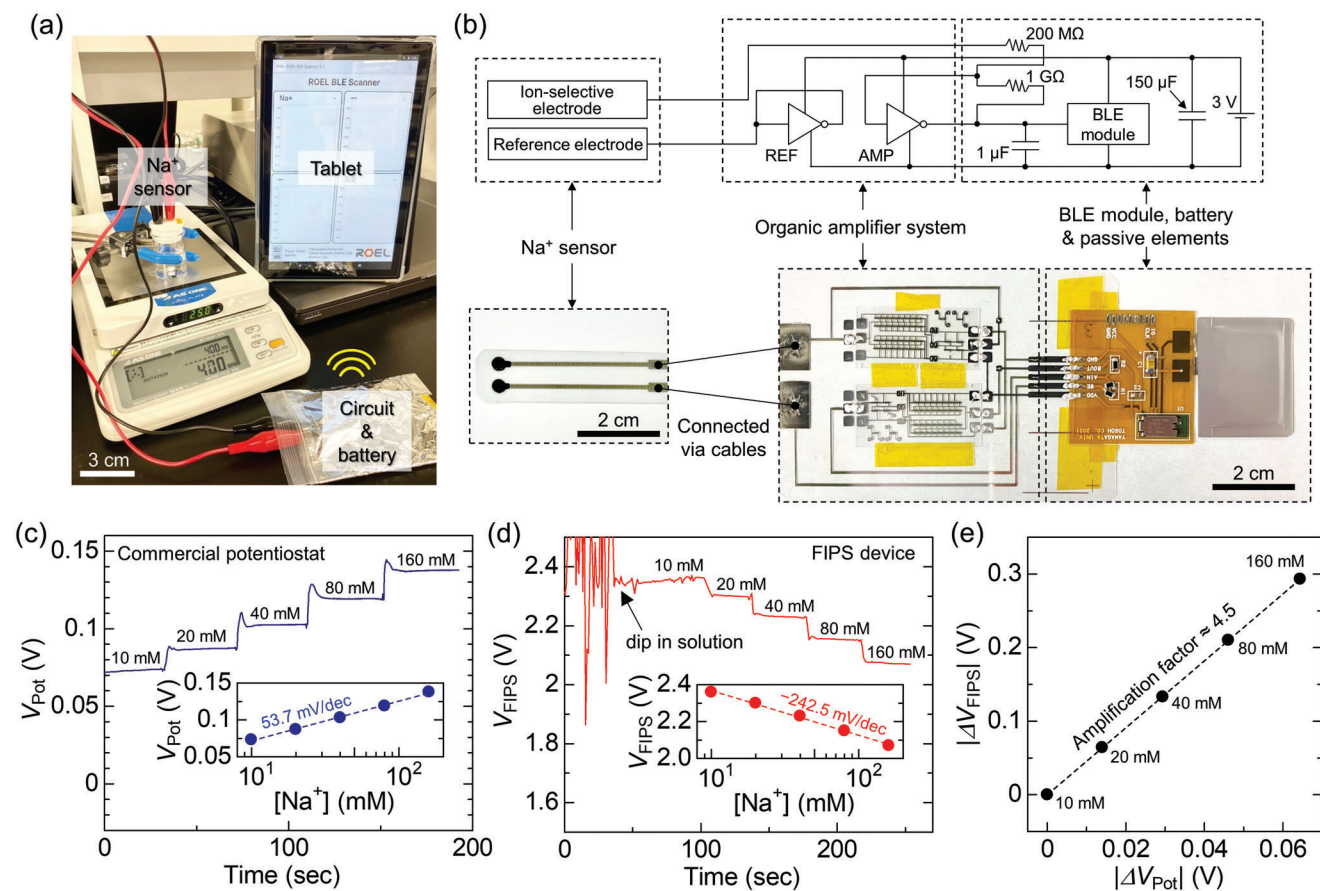


Figure 3. Demonstration of wireless Na^+ sensing with the FIPS device. a) Photograph of the entire experimental system. b) Circuit diagram and photograph of the flexible integrated potentiometric sensor (FIPS) device. Potentiometric responses obtained using c) a commercial potentiostat and d) the FIPS device. Concentration of the solution was changed stepwise by adding concentrated NaCl aqueous solution. The inset indicates the calibration. e) Absolute values of V_{FIPS} change ($|\Delta V_{\text{FIPS}}|$) versus those of V_{Pot} change ($|\Delta V_{\text{Pot}}|$) extracted from (c) and (d). The slope from least squares fitting ($\Delta V_{\text{FIPS}}/\Delta V_{\text{Pot}}$) corresponds to the amplification factor of the amplifier.

combinable with a BLE module were realized based on dual threshold technology, a voltage buffer, and dual-gate structure. The sensitivity of the Na^+ sensors was improved from 53.7 to 242.5 mV dec^{-1} (by a factor of 4.5) by the organic amplifier, and the data was transmitted to a tablet via the 2.4-GHz BLE wireless communication without significant signal attenuation. By replacing the passive elements and the battery with fully printed ones (printable resistors,^[37] printable capacitors,^[38] printable batteries^[39]), we can envision a BLE-module-detachable, printed smart patch for in situ cloud-based data analysis in the field of healthcare, sports, and medicals.

4. Experimental Section

Fabrication of Organic Semiconductor Devices: 2,7-dihexyl-dithieno[2,3-d;2',3'-d']benzo[1,2-b;4,5-b']dithiophene (DTBDT- C_6) was synthesized in the reported method.^[12] Except DTBDT- C_6 , all materials were used as received without further purification. 100- μm -thick polyethylene naphthalate (PEN, Teonex Q65HA, DuPont de Nemours, Inc.) films were used as substrates without a cleaning process. Bottom-gate electrodes and interconnections were printed by an inkjet printer (DMP-2831, Fujifilm) with silver nanoparticle (AgNP) ink in hydrocarbon-based solution (NPS-

JL, average particle size ≈ 5 nm, Harima Chemicals), followed by sintering at 120 $^\circ\text{C}$ for 30 min in an air ambient. The linewidth, thickness, and root-mean-square (RMS) roughness of the resultant electrodes was typically 180 μm , 30–100 nm, and 6 nm, respectively. A parylene dielectric layer was deposited by a chemical vapor deposition (CVD) method using source dimers (0.2 g, diX-SR, KISCO, Ltd.). The thickness and RMS roughness of the resultant parylene layer were 100 and 2 nm, respectively. Source and drain electrodes were subsequently printed and sintered in the same manner as the bottom-gate electrodes. To form lyophobic bank layers (200 nm thick), fluorinated polymer (1 wt.%, Teflon AF1600, DuPont de Nemours, Inc.) dissolved in a perfluorocarbon solvent (Fluorinert FC-43, 3 M Co.) were printed by a syringe dispenser system (Image Master 350 PC, MUSASHI Engineering). The surfaces of the silver source and drain electrodes were covered with self-assembled monolayers of pentafluorobenzethiol (PFBT, Tokyo Chemical Industry) by immersing the substrates in a solution of PFBT (3×10^{-2} M) in 2-propanol for 5 min at room temperature, followed by rinse with pure 2-propanol. This treatment increased the work-function of the electrodes from 4.7 to 5.4 eV and improved the injection of hole carriers to the p-type organic semiconductors. P-type organic semiconductor (OSC) solutions of 2,7-dihexyl-dithieno[2,3-d;2',3'-d']benzo[1,2-b;4,5-b']dithiophene (0.6 wt.%, DTBDT- C_6 , Tosoh Corporation) or 1,4,8,11-tetramethyl-6,13-bis(triethylsilyl)ethynylpentacene (0.6 wt.%, TMTES-p, Ossila, Ltd.) and polystyrene (0.2 wt.%, $M_w \approx 280000$, Sigma-Aldrich) as a binder in 1,2,3,4-tetrahydronaphthalene (tetralin) were prepared respectively. The

OSC solutions were printed onto the area defined by the bank layer using a syringe dispenser system, while keeping the substrate and nozzle temperatures at 100 and 30 °C, respectively, followed by annealing at 100 °C in an air ambient for 15 min to remove residual solvent. A parylene layer as an encapsulation/dielectric layer (1 μm thick) was subsequently formed by the CVD method using the source dimers (2 g). Finally, top-gate electrodes and contact pads were printed and sintered in the same manner as the bottom-gate electrodes except sintering temperature at 100 °C for 30 min.

Fabrication of Sodium Ion Sensors: All materials were used as received without further purification. The 100-μm-thick PEN films were used as substrates without a cleaning process. Electrodes for both ion-selective electrode (ISE) and reference electrode (RE) were printed by the inkjet printer with the AgNP ink, followed by sintering at 120 °C for 30 min in an air ambient. Carbon black solution was prepared by dissolving carbon black paste (5 mL, JELCON CH-8, Jujo Chemical Co., Ltd.) in propylene glycol monomethyl ether acetate (5 mL, PGMEA). The carbon black solution was subsequently coated onto the printed silver electrode,^[40] followed by sintering process of 120 °C for 30 min in an air ambient, to form an ion-to-electron transducer for the ISE^[41] or to improve potential stability of the RE under variation in chloride ion concentration.^[42] The resultant thickness of the carbon black layer was typically 5–10 μm. In order to define the area (3 mm diameter) of the following ion-selective membrane and liquid junction layer, lyophobic bank layers (10 μm thick) of a fluorinated polymer (5 wt.%, Teflon AF1600, DuPont de Nemours, Inc.) dissolved in a perfluorocarbon solvent (Fluorinert FC-43, 3 M Co.) were coated in the vicinity of the carbon black layer, followed by annealing at 120 °C for 30 min in air ambient. Sodium-ion-selective solution was prepared by dissolving sodium ionophore X (6 mg, Sigma–Aldrich), sodium tetrakis[3,5-bis(trifluoromethyl)phenyl]borate (3.3 mg, Sigma–Aldrich) as anion excluder, poly(vinyl chloride) (198 mg, Sigma–Aldrich) and bis(2-ethylhexyl)sebacate (431.4 μL, Wako Pure Chemical Industries) as plasticizer in cyclohexanone (2.1 mL).^[40] To form a sodium-ion-selective membrane (ISM), the sodium-ion-selective solution (4 μL) was drop-casted onto the carbon black surface whose area was defined by the bank for ISE, followed by a drying process of 40 °C for 30 min in air ambient. Liquid junction solution was prepared by dissolving poly(vinyl butyral) (79.1 mg, Sigma–Aldrich), NaCl (50 mg, Wako Pure Chemical Industries) in methanol (1 mL).^[43] To form liquid junction layer (LQJ), the liquid junction solution (4 μL) was finally drop-casted onto the carbon black surface whose area was defined by the bank for RE, followed by a drying process of room temperature in air ambient overnight. The resulting thickness of the ISM and LQJ was typically 80 μm and 40–80 μm, respectively. The fabricated sodium sensors were stored in electrolyte aqueous solution (1 × 10⁻¹ M NaCl, 1 × 10⁻² M KCl, 5 × 10⁻³ M NH₄Cl) at room temperature.

Assembly of Flexible Integrated Potentiometric Sensor (FIPS) devices: The sodium ion sensor and the organic amplifiers were connected via cables. Inorganic elements such as resistors, capacitors, and BLE modules (EYSGJNZWY, TAIYO YUDEN Co., Ltd.) were soldered on a polyimide film substrate with Cu interconnections. The inorganic elements were connected with the organic amplifiers and a 3-V sheet-type battery (CF052722U(N), FDK Corporation) via Ag paste (DOTITE D-500, Fujikura Kasei Co., Ltd.).

Characterization of Organic Semiconductor Devices: The capacitance of the dielectric and the CV characteristics of the OTFTs were measured using an LCR meter (ZM2376, NF). The electrical characteristics of the OTFTs and amplifier circuits were measured using a semiconductor parameter analyzer (4200A SCS, Keithley). A light-shielding test was performed using a white LED. The distance between OTFT devices and the LED was ≈8.5 cm and the measured illuminance was ≈66 000 lx. All electrical measurements were carried out in an air ambient. Optical microscope images of the devices were obtained using a digital microscope (VHX-7000, Keyence).

Potentiometric Measurements: The Na⁺ sensors were dipped in electrolyte aqueous solution (1 × 10⁻¹ M NaCl, 1 × 10⁻² M KCl, 5 × 10⁻³ M NH₄Cl) for at least 12 h before potentiometric measurements to stabilize their potential. The primary potentiometric measurements were carried out using a potentiostat (electrochemical analyzer, ALS612E, BAS). During the measurements, the subject solution was stirred at 400 rpm and

kept at room temperature. Demonstration of the FIPS device operation was carried out in a similar manner as the primary potentiometric measurements by replacing a commercial potentiostat with the FIPS devices. A tablet with a custom-developed application was used for receiving, displaying, and storing data from the FIPS devices.

Supporting Information

Supporting Information is available from the Wiley Online Library or from the author.

Acknowledgements

The authors gratefully acknowledge Mr. M. Kusumoto, and Mr. T. Kurit-subo for the technical support and valuable discussions.

Conflict of Interest

The authors declare no conflict of interest.

Data Availability Statement

The data that support the findings of this study are available from the corresponding author upon reasonable request.

Keywords

dual-gate, dual threshold, ion sensors, organic electronics, organic semiconductors, organic thin-film transistors, printed electronics

Received: June 14, 2023

Revised: July 28, 2023

Published online:

- [1] J. Wiklund, A. Karakoç, T. Palko, H. Yiğitler, K. Ruttik, R. Jäntti, J. Paltakari, *J. Manuf. Mater. Process.* **2021**, 5, 89.
- [2] T. Sekitani, U. Zschieschang, H. Klauk, T. Someya, *Nat. Mater.* **2010**, 9, 1015.
- [3] K. Fukuda, Y. Takeda, Y. Yoshimura, R. Shiwaku, L. T. Tran, T. Sekine, M. Mizukami, D. Kumaki, S. Tokito, *Nat. Commun.* **2014**, 5, 4147.
- [4] T. Minari, Y. Kanehara, C. Liu, K. Sakamoto, T. Yasuda, A. Yaguchi, S. Tsukada, K. Kashizaki, M. Kanehara, *Adv. Funct. Mater.* **2014**, 24, 4886.
- [5] N. Matsuhisa, M. Kaltenbrunner, T. Yokota, H. Jinno, K. Kuribara, T. Sekitani, T. Someya, *Nat. Commun.* **2015**, 6, 7461.
- [6] T. Sekitani, T. Yokota, K. Kuribara, M. Kaltenbrunner, T. Fukushima, Y. Inoue, M. Sekino, T. Isoyama, Y. Abe, H. Onodera, T. Someya, *Nat. Commun.* **2016**, 7, 11425.
- [7] M. Sugiyama, T. Uemura, M. Kondo, M. Akiyama, N. Namba, S. Yoshimoto, Y. Noda, T. Araki, T. Sekitani, *Nat. Electron.* **2019**, 2, 351.
- [8] S. Wang, J. Xu, W. Wang, G. N. Wang, R. Rastak, F. Molina-Lopez, J. W. Chung, S. Niu, V. R. Feig, J. Lopez, T. Lei, S. Kwon, Y. Kim, A. M. Fodeh, A. Enrlich, A. Gasperini, Y. Yun, B. Murmann, J. B.-H. Tok, Z. Bao, *Nature* **2018**, 555, 83.
- [9] T. Yokota, Y. Inoue, Y. Terakawa, J. Reeder, M. Kaltenbrunner, T. Ware, K. Yang, K. Mabuchi, T. Murakawa, M. Sekino, W. Voit, T. Sekitani, T. Someya, *Proc. Natl. Acad. Sci. USA* **2015**, 112, 14533.

- [10] R. Shiwaku, H. Matsui, K. Nagamine, M. Uematsu, T. Mano, Y. Maruyama, A. Nomura, K. Tsuchiya, K. Hayasaka, Y. Takeda, T. Fukuda, D. Kumaki, S. Tokito, *Sci. Rep.* **2018**, *8*, 6368.
- [11] R. Shiwaku, H. Matsui, K. Nagamine, M. Uematsu, T. Mano, Y. Maruyama, A. Nomura, K. Tsuchiya, K. Hayasaka, Y. Takeda, T. Fukuda, D. Kumaki, S. Tokito, *Sci. Rep.* **2018**, *8*, 3922.
- [12] K. Fukuda, T. Minamiki, T. Minami, M. Watanabe, T. Fukuda, D. Kumaki, S. Tokito, *Adv. Electron. Mater.* **2015**, *1*, 1400052.
- [13] W. Tang, Y. Fu, Y. Huang, Y. Li, Y. Song, X. Xi, Y. Yu, Y. Su, F. Yan, X. Guo, *npj Flexible Electron.* **2022**, *6*, 18.
- [14] I. Nausieda, K. K. Ryu, D. D. a He, A. I. Akinwande, V. Bulovic, C. G. Sodini, *IEEE Trans. Electron Devices* **2010**, *57*, 3027.
- [15] I. Nausieda, K. K. Ryu, D. D. a He, A. I. Akinwande, V. Bulovic, C. G. Sodini, *IEEE Trans. Electron Devices* **2011**, *58*, 865.
- [16] R. Shiwaku, H. Matsui, K. Hayasaka, Y. Takeda, T. Fukuda, D. Kumaki, S. Tokito, *Adv. Electron. Mater.* **2017**, *3*, 1600557.
- [17] K. Taguchi, T. Uemura, N. Namba, A. Petritz, T. Araki, M. Sugiyama, B. Stadlober, T. Sekitani, *Adv. Mater.* **2021**, *33*, 2104446.
- [18] S. H. Kim, H. R. Hwang, H. J. Kwon, J. Jang, *Appl. Phys. Lett.* **2012**, *100*, 053302.
- [19] M. Kitamura, Y. Kuzumoto, S. Aomori, M. Kamura, J. H. Na, Y. Arakawa, *Appl. Phys. Lett.* **2009**, *94*, 083310.
- [20] C. A. Lee, S. H. Jin, K. D. Jung, J. D. Lee, B.-G. Park, *Solid-State Electron.* **2006**, *50*, 1216.
- [21] R. Shiwaku, Y. Yoshimura, Y. Takeda, K. Fukuda, D. Kumaki, S. Tokito, *Appl. Phys. Lett.* **2015**, *106*, 053301.
- [22] A. Arnal, C. Martínez-Domingo, S. Ogier, L. Terés, E. Ramon, *Crystals* **2019**, *9*, 333.
- [23] S. Iba, T. Sekitani, Y. Kato, T. Someya, H. Kawaguchi, M. Takamiya, T. Sakurai, S. Takagi, *Appl. Phys. Lett.* **2005**, *87*, 023509.
- [24] S. Lee, T. Yokota, T. Someya, *Jpn. J. Appl. Phys.* **2017**, *56*, 04CL01.
- [25] H. Fuketa, K. Yoshioka, T. Yokota, W. Yukita, M. Koizumi, M. Sekino, T. Sekitani, M. Takamiya, T. Someya, T. Sakurai, 2014 IEEE Int. Solid-State Circuits Conf. Digest of Technical Papers (ISSCC), IEEE, Piscataway, NJ **2014**, p. 490.
- [26] V. Fiore, P. Battiato, S. Abdinia, S. Jacobs, I. Chartier, R. Coppard, G. Klink, E. Cantatore, E. Ragonese, G. Palmisano, *IEEE Trans. Circuits Syst. I: Regul. Pap.* **2015**, *62*, 1668.
- [27] J. M. Shaw, P. F. Seidler, *IBM J. Res. Dev.* **2001**, *45*, 3.
- [28] Y. Yan, Y. Zhao, Y. Liu, *J. Polym. Sci.* **2022**, *60*, 311.
- [29] P. Gao, D. Beckmann, H. N. Tsao, X. Feng, V. Enkelmann, M. Baumgarten, W. Pisula, K. Müllen, *Adv. Mater.* **2009**, *21*, 213.
- [30] G. R. Llorente, M.-B. Dufourg-Madec, D. J. Crouch, R. G. Pritchard, S. Ogier, S. G. Yeates, *Chem. Commun.* **2009**, 3059.
- [31] T.-C. Huang, K. Fukuda, C.-M. Lo, Y.-H. Yeh, T. Sekitani, T. Someya, K.-T. Cheng, *IEEE Trans. Electron Devices* **2011**, *58*, 141.
- [32] R. Shiwaku, M. Tamura, H. Matsui, Y. Takeda, T. Murase, S. Tokito, *Appl. Sci.* **2018**, *8*, 1341.
- [33] S. Baek, H. Matsui, T. Mano, J. A. Park, Y. Jo, Y. Lee, S. Tokito, J. Kwon, S. Jung, *Biosens. Bioelectron.* **2023**, *222*, 114958.
- [34] H. Matsui, K. Hayasaka, Y. Takeda, R. Shiwaku, J. Kwon, S. Tokito, *Sci. Rep.* **2018**, *8*, 8980.
- [35] J. Kwon, Y. Takeda, R. Shiwaku, S. Tokito, K. Cho, S. Jung, *Nat. Commun.* **2019**, *10*, 54.
- [36] C. Jiang, *Crystals* **2020**, *10*, 727.
- [37] S. Jung, A. Sou, E. Gili, H. Siringhaus, *Org. Electron.* **2013**, *14*, 699.
- [38] R. Worsley, L. Pimpolari, D. Mcmanus, N. Ge, R. Ionescu, J. A. Wittkopf, A. Alieva, G. Basso, M. Macucci, G. Iannaccone, K. S. Novoselov, H. Holder, G. Fiori, C. Casiraghi, *ACS Nano* **2019**, *13*, 54.
- [39] K.-H. Choi, D. B. Ahn, S.-Y. Lee, *ACS Energy Lett.* **2018**, *3*, 220.
- [40] M. Bariya, Z. Shahpar, H. Park, J. Sun, Y. Jung, W. Gao, H. Y. Y. Nyein, T. S. Liaw, L.-C. Tai, Q. P. Ngo, M. Chao, Y. Zhao, M. Hettick, G. Cho, A. Javey, *ACS Nano* **2018**, *12*, 6978.
- [41] Y. Shao, Y. Ying, J. Ping, *Chem. Soc. Rev.* **2020**, *49*, 4405.
- [42] Y. Huang, T. Wang, Z. Xu, E. Hughes, F. Qian, M. Lee, Y. Fan, Y. u Lei, C. Brückner, B. Li, *Environ. Sci. Technol.* **2019**, *53*, 3140.
- [43] A. M. Zamarayeva, N. A. D. Yamamoto, A. Toor, M. E. Payne, C. Woods, V. I. Pister, Y. Khan, J. W. Evans, A. C. Arias, *APL Mater.* **2020**, *8*, 100905.